

Coherent Interferometric Imaging in Clutter

Liliana Borcea*, George Papanicolaou†, Chrysoula Tsogka‡

(January 5, 2006)

ABSTRACT

Coherent interferometry is an array imaging method in which we back propagate, or migrate, crosscorrelations of the traces over appropriately chosen space-time windows, rather than the traces themselves. The size of the space-time windows is critical and depends on two parameters. One is the decoherence frequency, which is proportional to the reciprocal of the delay spread in the traces produced by the clutter. The other is the decoherence length, which also depends on the clutter. As is usual, the clutter is modeled by random fluctuations in the medium properties. In isotropic clutter the decoherence length is typically much smaller than the array aperture. In layered random media the decoherence length along the layers can be quite large. We show that when the crosscorrelations of the traces are calculated adaptively then coherent interferometry can provide images that are statistically stable relative to small scale clutter in the environment. This means that the images we obtain are not sensitive to the detailed form of the clutter. They only depend on its overall statistical properties. However, clutter does reduce the resolution of the images by

*Computational and Applied Mathematics, MS 134, Rice University, 6100 Main Street, Houston, TX 77005-1892.(borcea@caam.rice.edu)

†Department of Mathematics, Stanford University, Stanford, CA 94305.
(papanico@math.stanford.edu)

‡Department of Mathematics, University of Chicago, Chicago, IL 60637.
(tsogka@math.uchicago.edu)

blurring. We show how the amount of blurring can be minimized by using adaptive interferometric imaging algorithms, and discuss the relation between the coherence properties of the array data and the loss in resolution caused by the blurring.

INTRODUCTION

In imaging, and in seismic imaging in particular, we wish to estimate the location of one or more underground sources or reflecting structures with a passive or an active array of receivers, respectively, lying on the surface, as shown in Figure 1, left and right.

Imaging of sources or reflectors in smooth background media is done efficiently with Kirchhoff migration (Claerbout and Doherty, 1972; Schultz and Claerbout, 1978; Claerbout, 1985; Beylkin, 1985; Beylkin and Burridge, 1990; Nolan and Symes, 1997; Kroode et al., 1998; Bleistein et al., 2001; Stolk and deHoop, 2002) when the background propagation velocity is known or can be estimated (Carazzone and Symes, 1991; Symes, 1991; Symes, 1993; Gockenbach, 1994; Stolk and Symes, 2003). However, in addition to the large scale features of the subsurface wave velocity, which are not known but can be estimated, there are small scale inhomogeneities (clutter) that can have a more or less layered structure, as is often the case in seismic imaging, (see Figure 2) or a more isotropic one as in ultrasonic imaging inside concrete (see Figure 3), etc. In cluttered environments where there is significant multiple scattering, or multipathing, migration, such as travel time or Kirchhoff migration, does not work well. This is because it relies on relatively clean arrivals. However, when there is clutter the recorded time traces have long and noisy codas that come from the multiple scattering by the inhomogeneities. Images obtained with Kirchhoff migration look noisy and unstable with respect to the realization of the clutter, that is, different realizations of the clutter with the same statistical properties produce different images.

We have shown in (Borcea et al., 2003; Borcea et al., 2005b) (see also (Chan et al., 1999)) that to stabilize the imaging process in cluttered environments one should do interferometric migration. This means that it is the crosscorrelations of the traces, the interferograms, that should be migrated, not the traces themselves.

Interferometric methods, that is, methods that use crosscorrelations of traces, have been used before in various contexts: (1) In daylight seismic imaging (Claerbout, 1968; Cole, 1995; Rickett and Claerbout, 1999), passive array traces at one or more receivers are crosscorrelated for the purpose of simulating reflection data. This was done first in horizontally layered media (Claerbout, 1968), and later for more general velocity models (Cole, 1995; Rickett and Claerbout, 1999). (2) Crosscorrelations are also used in (Lobkis and Weaver, 2001; Snieder, 2004), where passive traces at two receivers are crosscorrelated to provide an estimate of the Green's function between the two receiver locations. (3) In (Schuster et al., 2004), the daylight imaging approach (Claerbout, 1968; Cole, 1995; Rickett and Claerbout, 1999) is extended to the estimation of subsurface sources and receivers. In these works the aim is not to estimate the location of strong sources or reflectors but rather to extract information about the medium between the two receivers, the Green's function in favorable circumstances. However, in (Borcea et al., 2003; Borcea et al., 2005b), we have presented a detailed study of interferometry as a statistically stable imaging method for sources and reflectors in clutter.

Stable interferometric imaging in clutter works with crosscorrelations of nearby traces that are separated by distances no greater than the decoherence length, which is a clutter dependent parameter. This decoherence length is typically much smaller than the array aperture in isotropic clutter, as in Figure 3, but it can increase in anisotropic media and even become unbounded in the extreme case of a finely layered medium with the layers parallel to the surface. Because in imaging we do not know the clutter, it is important to be able to estimate the decoherence length from the array data and this can be done well during the image formation process, as we

explain in (Borcea et al., 2003; Borcea et al., 2005b).

A form of interferometric imaging, also known as matched field processing (Bucker, 1976; Krolik, 1992; Baggeroer et al., 1993), is a very efficient way of stabilizing images when there is clutter, as well as reducing instrument noise, but it has no range (depth) resolution at all (because it crosscorrelates the full traces without time windowing), except for what comes from geometric triangulation when multiple or extended arrays are available. Of course, matched field interferometry can be coupled with an arrival time analysis, but this can be tricky in cluttered media where late arrivals from deep reflectors are buried in the coda of earlier arrivals. What is shown in (Borcea et al., 2005b) is that range resolution can be recovered if the crosscorrelations are computed over appropriately chosen time windows that separate information from different ranges in the cluttered medium. The size of the time window is critical in achieving statistical stability and it depends on another key clutter dependent parameter: the decoherence frequency, which is proportional to the reciprocal of the delay spread in the traces. We call the crosscorrelations of traces over such windows coherent interferograms and by coherent interferometric imaging we mean the migration of the coherent interferograms.

The coherent interferograms achieve considerable cancellation of the random phases in our data (i.e., diminishing of coda effects). The process of calculating space-time windowed crosscorrelations can also be viewed as an efficient statistical smoothing technique (Priestley, 1981; Borcea et al., 2005a), if we know the clutter dependent decoherence length and frequency. If we underestimate the size of the decoherence parameters, by taking a very fine space-frequency segmentation of our data, then we have a stable result which is overly smoothed at the expense of resolution. On the other hand, overestimating the decoherence length and frequency does not provide enough smoothing and the images are noisy and unstable. There is, therefore, a delicate balance between achieving stable and well resolved images, which requires a robust estimation of the clutter dependent decoherence length and

frequency.

In principle, the decoherence parameters can be determined directly from the traces, with some good statistical signal processing. However, since these parameters affect the quality of the image in such an important way, we should estimate them during the image formation process with an optimization criterion that seeks a compromise between smoothing and resolution. This leads to what we call adaptive coherent interferometry, where during the formation of the coherent interferograms we adapt the space-frequency segmentation of our data to obtain the best quality image. Naturally, the effect of the clutter is felt in our final image, which is a blurred version of the Kirchhoff migration image that one would obtain if the clutter were absent. The point is, however, that through adaptive coherent interferometry we obtain the sharpest stable images that we can get in clutter and the amount of blurring can be quantified explicitly and diminished subsequently with a deblurring process (Borcea et al., 2005a).

In this paper, we review our results in (Borcea et al., 2005b) in both coherent and adaptive coherent interferometry, in two very different cluttered media: First, we look at isotropic clutter with weak fluctuations of the wave velocity and long propagation distances so as to have significant multiple scattering that is mostly in the forward direction. We then consider the case of finely layered media with strong backscattering of the waves by the layers. In both cases we find that adaptive coherent interferometry works very well and gives much better images than the usual (prestack) Kirchhoff migration. This suggests that this imaging method could be used in general, whenever there is significant clutter.

INTERFEROMETRIC IMAGING IN CLUTTER

Formulation of the problem

In the simplest case of imaging a point source at an unknown, underground location \mathbf{y} we suppose that a pulse

$$f(t) = e^{-i\omega_o t} f_B(t), \quad (1)$$

of carrier frequency ω_o and bandwidth B , is emitted from \mathbf{y} and propagates to the surface where we record the time traces of the acoustic pressure P ,

$$P(\mathbf{x}_r, t), \quad \mathbf{x}_r \in \mathcal{A}, \quad t \in [t_m, t_M], \quad r = 1, \dots, N, \quad (2)$$

at an array \mathcal{A} of N transducers, over a time window $[t_m, t_M]$. If we have many sources, or a distributed one of support \mathcal{D} , we take for simplicity the ideal situation of the same pulse in equation 1 being sent simultaneously from all the source points, with possibly variable intensity. In either case, we wish to image the support of the sources, given the array data in equation 2.

When imaging reflectors, the pulse $f(t)$ is sent from $\mathbf{x}_s \in \mathcal{A}$, $s = 1, \dots, N_S$, and we record the scattered echoes

$$P(\mathbf{x}_r, t; \mathbf{x}_s), \quad \mathbf{x}_r \in \mathcal{A}, \quad t \in [t_m, t_M], \quad r = 1, \dots, N, \quad (3)$$

at the array \mathcal{A} on the surface. The inverse problem is to image the support of the reflectors from the array data in equation 3. We base our imaging method on the single scattering (Born) approximation of the waves by the unknown reflectors. We do not, however, assume that only single scattering results from the clutter. In fact, an important feature of our work is that we can image in cluttered environments in regimes with significant multipathing, where the recorded traces have long and noisy codas.

The subsurface sound velocity $c(\mathbf{x})$ consists of a smooth part $c_o(\mathbf{x})$, that we assume known, of the fluctuations (i.e., the clutter) that we do not know and we model as a random process, and of the reflectors that we wish to image. We assume here that the contrast between the reflectors and the known background profile $c_o(\mathbf{x})$ is big (infinite in the simulations considered in this paper) while the clutter fluctuations are smaller (typically their strength is of the order of 3% for isotropic clutter and 30% for the layered case).

If we do not know $c_o(\mathbf{x})$, we can estimate it using, for example, the differential semblance approach (Carazzone and Symes, 1991; Symes, 1991; Symes, 1993; Gockenbach, 1994; Stolk and Symes, 2003). Obviously, we cannot assume that we know the clutter, and we cannot hope to estimate it in all its details. Instead, we think of the clutter as a realization of a stationary random process with standard deviation σ and correlation lengths (size of inhomogeneities) l_x and l_z in the cross-range and range directions, respectively. Note that we use in this paper the terms cross-range and range to refer to what is usually called lateral position and depth in exploration geophysics. See Figure 3 for an illustration of an isotropic clutter, with $l_x = l_z = 1.5$ m, constant mean sound speed $c_o = 3$ km/s and fluctuations strength $\sigma = 3\%$. The size of the domain is $270 \text{ m} \times 270 \text{ m}$. Examples of horizontally layered media are given in Figure 8, where the fluctuations are stronger, $\sigma = 30\%$, the cross-range correlation length l_x is infinite and the width of the layers is roughly $l_z = 30$ m. The size of the domain is $6 \text{ km} \times 24 \text{ km}$.

Note that since our interest is in assessing the effect of the clutter on imaging, we take a constant background $c_o(\mathbf{x}) = c_o$ and we avoid dealing with reflections at the surface by using a perfect matching condition of the sound speed there.

The interferometric imaging function and its connection to time reversal

In Kirchhoff migration we form an image by migrating traces, equation 2 or equation 3, to a search point \mathbf{y}^s where we expect that our sources or reflectors lie. Assuming that the medium is smooth, that is, the speed changes over distances that are long compared with wavelengths λ , we can use geometrical optics to migrate to \mathbf{y}^s . Explicitly, we evaluate $P(\mathbf{x}_r, t)$ at the travel time $\tau(\mathbf{x}_r, \mathbf{y}^s)$, which in a homogeneous medium with constant propagation speed c_o is $|\mathbf{x}_r - \mathbf{y}^s|/c_o$, and then sum over the array to get the imaging function

$$\mathcal{I}^{\text{KM}}(\mathbf{y}^s) = \sum_{r=1}^N P(\mathbf{x}_r, \tau(\mathbf{x}_r, \mathbf{y}^s)) \quad (4)$$

for passive array imaging. In case of reflection data, with illumination from location \mathbf{x}_s in the active array \mathcal{A} , we have

$$\mathcal{I}^{\text{KM}}(\mathbf{y}^s) = \sum_{r=1}^N P(\mathbf{x}_r, \tau(\mathbf{x}_r, \mathbf{y}^s) + \tau(\mathbf{x}_s, \mathbf{y}^s); \mathbf{x}_s). \quad (5)$$

When the medium is cluttered but known, we can migrate by means of the Green's function $G(\mathbf{x}, \mathbf{y}^s, t)$ in the clutter. To simplify our arguments, let us assume from now on that we image a small source at unknown location \mathbf{y} . Extensions to distributed sources and reflectors are straightforward and we show numerical results for these cases later on. The migration by means of the Green's function in clutter gives

$$\begin{aligned} \mathcal{I}^{\text{TR}}(\mathbf{y}^s) &= \sum_{\mathbf{x}_r \in \mathcal{A}} \int_{|\omega - \omega_o| \leq B} d\omega \widehat{P}(\mathbf{x}_r, \omega) \overline{\widehat{G}(\mathbf{x}_r, \mathbf{y}^s, \omega)} \\ &= \sum_{\mathbf{x}_r \in \mathcal{A}} \int_{|\omega - \omega_o| \leq B} d\omega \widehat{f}_B(\omega - \omega_o) \widehat{G}(\mathbf{x}_r, \mathbf{y}, \omega) \overline{\widehat{G}(\mathbf{x}_r, \mathbf{y}^s, \omega)}, \end{aligned} \quad (6)$$

where hats denote Fourier transform and the bar indicates complex conjugate. The function $\mathcal{I}^{\text{TR}}(\mathbf{y}^s)$ represents the field at \mathbf{y}^s when the array time reverses the signals received and re-emits them in the medium, so we call it the time-reversal function. It is the ideal imaging function for two reasons: (1) it is usually self-averaging, especially in broad-band regimes (Clouet and Fouque, 1997; Blomgren et al., 2002; Solna, 2002; Bal

et al., 2002; Bal and Ryzhik, 2003; Fouque and Solna, 2003; Papanicolaou et al., 2004; Fouque et al., 2005) and (2) it focuses much better in cluttered media¹ (Fink, 1993; Derode et al., 1995; Fink, 1997; Song et al., 1999; Fink et al., 2000; Blomgren et al., 2002; Bal et al., 2002; Bal and Ryzhik, 2003), because by scattering from the clutter the waves are distributed over a larger part of the medium, and behave as if they came from a larger array. The function \mathcal{I}^{TR} is self-averaging because when \mathbf{y}^s is near \mathbf{y} there is significant random phase cancellation in the product $\widehat{G}(\mathbf{x}_r, \mathbf{y}, \omega) \overline{\widehat{G}(\mathbf{x}_r, \mathbf{y}^s, \omega)}$ and so, after integrating over the bandwidth, we get an efficient delay spread (coda) reduction that leads to sharp and stable maxima at the support of the source.

The problem with \mathcal{I}^{TR} is that we do not know the clutter (i.e. $G(\mathbf{x}_r, \mathbf{y}^s, t)$) in detail. As a matter of fact, it is because we do not know the clutter that we model it as a random process. Then, migrating the data in the homogeneous medium or with some “approximation” of the Green’s function will not remove the coda and the resulting images are noisy and unreliable. However, we can reduce the delay spread without knowing the clutter by crosscorrelating nearby traces to produce the interferograms, which we then migrate to the search location \mathbf{y}^s . This gives the interferometric imaging point spread function

$$\begin{aligned} \mathcal{I}^{\text{INT}}(\mathbf{y}^s; X_d) = & \sum_{\substack{\mathbf{x}_{r'}, \mathbf{x}_r \in \mathcal{A} \\ |\mathbf{x}_{r'} - \mathbf{x}_r| \leq X_d}} P(\mathbf{x}_r, t) \star_t P(\mathbf{x}_{r'}, -t) \Big|_{t=\tau(\mathbf{x}_r, \mathbf{y}^s) - \tau(\mathbf{x}_{r'}, \mathbf{y}^s)} = \\ & \sum_{\substack{\mathbf{x}_{r'}, \mathbf{x}_r \in \mathcal{A} \\ |\mathbf{x}_{r'} - \mathbf{x}_r| \leq X_d}} \int_{|\omega - \omega_o| \leq B} d\omega |\widehat{f}_B(\omega - \omega_o)|^2 \widehat{G}(\mathbf{x}_r, \mathbf{y}, \omega) \overline{\widehat{G}(\mathbf{x}_{r'}, \mathbf{y}, \omega)} e^{-i\omega[\tau(\mathbf{x}_r, \mathbf{y}^s) - \tau(\mathbf{x}_{r'}, \mathbf{y}^s)]}, \end{aligned} \quad (7)$$

where we restrict the cross-range offset over which we calculate the interferograms to the decoherence length X_d . If we crosscorrelate traces that are further apart, the resulting interferograms are as noisy as the traces themselves, with little coherent

¹This is true in most cluttered environments, but for example, in horizontally layered media, we do not get super-resolution because there is no cross-range diversity in the medium.

structure. Smoothing is the process by which such crosscorrelations are excluded from the interferometric imaging functional.

In view of the reciprocity of the Green's functions, we note a striking similarity between the time-reversal and the interferometric imaging functions in equation 6 and equation 7. This allows us to identify the decoherence length X_d as the cross-range focusing resolution in time-reversal. In cluttered media with rich cross-range diversity, such as the isotropic clutter in Figure 3, the time-reversal focal spot is rather small, certainly much smaller than most array apertures a (Fink, 1993; Derode et al., 1995; Fink, 1997; Song et al., 1999; Fink et al., 2000; Blomgren et al., 2002; Bal et al., 2002; Bal and Ryzhik, 2003). This means that interferometric imaging in clutter can work only with interferograms over small cross-range offsets and this puts significant limitations on its resolution, as we show next.

Resolution limits

It is well known that the range resolution of Kirchhoff migration images in a uniform medium with sound speed c_o is proportional to the distance traveled by the waves over the pulse width $T_p \sim \pi/B$ (Bleistein et al., 2001). Explicitly, we have range resolution $O(\pi c_o/B)$. The cross-range resolution is affected by the array aperture a and it is $O(\pi c_o L/(Ba))$, where L is the propagation distance (range) (Bleistein et al., 2001). A more general way to estimate the resolution limits is presented in (Sheng and Schuster, 2003).

In interferometric imaging in cluttered environments, it is not the array aperture that determines the cross-range resolution. It is the decoherence length X_d . This is because we cannot crosscorrelate traces that are further than X_d apart and get a stable image. Therefore, the cross-range resolution in clutter is $O(\pi c_o L/(BX_d))$ (Borcea et al., 2003; Borcea et al., 2005b) and, as expected, in media with rich cross-range diversity, the images are blurrier than what the deterministic Rayleigh

resolution theory predicts.

Because the interferograms are crosscorrelations of nearby traces, over the whole time interval, there is no direct arrival time information in $\mathcal{I}^{\text{INT}}(\mathbf{y}^s)$ and the range information is lost, unless we couple the interferometric imaging with an arrival time analysis (Borcea et al., 2002a; Borcea et al., 2002b; Borcea et al., 2003). Range resolution can also be retrieved by geometric triangulation, if large or multiple arrays are available. However, in many cases there is a much more efficient way of recovering range resolution. This is done by computing crosscorrelations of the traces *locally* in time, as we do in coherent interferometry.

COHERENT INTERFEROMETRIC IMAGING IN CLUTTER

In order to recover range resolution in interferometric imaging, we segment first the traces over time intervals of length T_d and then we calculate correlations locally in each time interval (Borcea et al., 2005b). This gives the coherent interferograms that we then migrate to the search point \mathbf{y}^s .

Let $\Omega_d = \pi/T_d$ and introduce the notation $\mathbf{x} = (\mathbf{x}^\perp, z)$ that distinguishes between the cross-range \mathbf{x}^\perp and range z of an arbitrary point \mathbf{x} in the three dimensional space. Assuming a nearly flat surface, the transducer locations are $\mathbf{x}_r = (\mathbf{x}_r^\perp, 0)$, so we change our notation in the traces and travel times as $P(\mathbf{x}_r, t) \rightsquigarrow P(\mathbf{x}_r^\perp, t)$ and $\tau(\mathbf{x}_r, \mathbf{y}^s) \rightsquigarrow \tau(\mathbf{x}_r^\perp, \mathbf{y}^s)$, for $r = 1, \dots, N$. We also introduce the midpoint and offset variables

$$\bar{\mathbf{x}}_r^\perp = \frac{\mathbf{x}_r^\perp + \mathbf{x}_{r'}^\perp}{2}, \quad \tilde{\mathbf{x}}_r^\perp = \mathbf{x}_{r'}^\perp - \mathbf{x}_r^\perp. \quad (8)$$

The coherent interferometric (CINT) imaging function is defined by

$$\begin{aligned} \mathcal{I}^{\text{CINT}}(\mathbf{y}^s, X_d, \Omega_d) = & \int_{|\bar{\omega} - \omega_o| \leq B} d\bar{\omega} \int_{-\Omega_d}^{\Omega_d} d\tilde{\omega} \sum_{\mathbf{x}_r^\perp \in \mathcal{A}} \sum_{\mathbf{x}_{r'}^\perp \in \mathcal{A}, |\tilde{\mathbf{x}}_r^\perp| \leq X_d} \hat{P} \left(\bar{\mathbf{x}}_r^\perp - \frac{\tilde{\mathbf{x}}_r^\perp}{2}, \bar{\omega} - \frac{\tilde{\omega}}{2} \right) \times \\ & \overline{\hat{P} \left(\bar{\mathbf{x}}_r^\perp + \frac{\tilde{\mathbf{x}}_r^\perp}{2}, \bar{\omega} + \frac{\tilde{\omega}}{2} \right)} \exp \left\{ i\bar{\omega} \left[\tau \left(\bar{\mathbf{x}}_r^\perp + \frac{\tilde{\mathbf{x}}_r^\perp}{2}, \mathbf{y}^s \right) - \tau \left(\bar{\mathbf{x}}_r^\perp - \frac{\tilde{\mathbf{x}}_r^\perp}{2}, \mathbf{y}^s \right) \right] \right\} \times \\ & \exp \left\{ i\frac{\tilde{\omega}}{2} \left[\tau \left(\bar{\mathbf{x}}_r^\perp + \frac{\tilde{\mathbf{x}}_r^\perp}{2}, \mathbf{y}^s \right) + \tau \left(\bar{\mathbf{x}}_r^\perp - \frac{\tilde{\mathbf{x}}_r^\perp}{2}, \mathbf{y}^s \right) \right] \right\}. \end{aligned} \quad (9)$$

Note that $\bar{\mathbf{x}}_r^\perp$ sweeps the array aperture whereas $\tilde{\mathbf{x}}_r^\perp$ is limited by the decoherence length X_d . Similarly, $\bar{\omega}$ sweeps the bandwidth while the offset frequency $\tilde{\omega}$ is limited by Ω_d , which is a frequency decoherence parameter that is analogous to X_d .

Assuming that X_d is small when scaled by the range, we can linearize the phase in equation 9 and write the time domain analogue of $\mathcal{I}^{\text{CINT}}$ (Borcea et al., 2005b)

$$\mathcal{I}^{\text{CINT}}(\mathbf{y}^s, X_d, T_d) = \sum_{\mathbf{x}_r^\perp \in \mathcal{A}} \sum_{\mathbf{x}_r^\perp \in \mathcal{A}, |\tilde{\mathbf{x}}_r^\perp| \leq X_d} \int_{|\bar{t} - \tau(\bar{\mathbf{x}}_r^\perp, \mathbf{y}^s)| \leq T_d} d\bar{t} \int_{|\bar{t} - \tilde{\mathbf{x}}_r^\perp \cdot \nabla_{\tilde{\mathbf{x}}_r^\perp} \tau(\bar{\mathbf{x}}_r^\perp, \mathbf{y}^s)| \leq T_p} d\tilde{t} \times \quad (10)$$

$$P(\bar{\mathbf{x}}_r^\perp - \frac{\tilde{\mathbf{x}}_r^\perp}{2}, \bar{t} - \frac{\tilde{t}}{2}) P(\bar{\mathbf{x}}_r^\perp + \frac{\tilde{\mathbf{x}}_r^\perp}{2}, \bar{t} + \frac{\tilde{t}}{2}),$$

where $T_d = \pi/\Omega_d$ is the decoherence time and $T_p = \pi/B$ is the pulse width. Note that equation 10 is not the exact transformation of equation 9, but rather its time domain analog. This is because cutoffs in frequency become sinc kernels in the time domain. In the numerical computations, we use the frequency domain version of the coherent interferometric functional.

It is now clear that there are two key parameters in coherent interferometry: the decoherence length X_d and the time segmentation T_d or its reciprocal, the decoherence frequency Ω_d . How long should T_d be? It should be long enough, to capture enough delay spread in the traces and then compress it, by the correlation. Then, the coherent interferograms will be smooth and their downward migration leads to stable results. However, the smoothing by time averaging over the windows of size T_d (see the \bar{t} integral in equation 10) comes at the expense of range resolution, which is now $O(c_o T_d) = O(\pi c_o / \Omega_d)$. Therefore, we should choose T_d as short as possible in order to get the best resolution and yet, maintain statistical stability. We explain how to do this in the adaptive coherent interferometry section.

The cross-range resolution in coherent interferometry comes from the integration over the time lag \tilde{t} and it is the same as in interferometry, $O(\pi L c_o / (B X_d))$.

Numerical results for coherent interferometry in isotropic random media

We present in this section results of numerical simulations for imaging with an active array configuration using the coherent interferometric functional. The numerical setup is shown in Figure 4 where the dimensions are given in terms of the central wavelength λ_0 . To image we use a linear array of 185 transducers located at depth $2\lambda_0$ and at distance $h = \lambda_0/2$ from each other. The object to be imaged is at range $L = 90\lambda_0$ and at zero cross-range, measured with respect to the center of the array. It is composed of three non penetrable disks of diameter λ_0 . The distance between the centers of these disks is $d = 6\lambda_0$. To simulate imaging in a cluttered medium, the scatterers are embedded in a heterogeneous background where the fluctuations in the sound speed $c(\mathbf{x})$ are modeled with random Fourier series that have mean $c_0 = 3$ km/s and two correlation functions: (i) a mono-scale Gaussian one,

$$R(x_1, x_2) = R(|x_1 - x_2|) = \exp(-|x_1 - x_2|^2/(2l^2)), \quad (11)$$

with correlation length $l = \lambda_0/2$ and (ii) a correlation function with a range of scale sizes,

$$R(x_1, x_2) = R(|x_1 - x_2|) = (1 + |x_1 - x_2|/l)\exp(-|x_1 - x_2|/l), \quad (12)$$

where $l = \lambda_0$. For large spatial frequencies, the spectrum of equation 12 has power law behavior as is typical in multiscale random media, and thus it gives a good and simple way to assess the effect of a range of scale sizes in the random medium (Uscinski, 1985).

The data recorded on the array correspond to the following experiment: One of the array elements sends a probing pulse $f(t)$ and the response of the medium is recorded at all array elements. The pulse used is a time derivative of a Gaussian with central frequency $\omega_0/(2\pi) = 1$ kHz and bandwidth 0.6 – 1.3 kHz (measured at 6 dB). With a mean propagation speed of 3 km/s the central wavelength is $\lambda_0 = 3$ m. The probing pulse is sent sequentially from three array elements: the central one, and two

others located at cross-range $23\lambda_0$ and $-23\lambda_0$, respectively.

To generate the data we solve the acoustic wave equation, formulated as a first order in time velocity-pressure system, using a mixed finite element method (Bécache et al., 2000). The propagation medium is considered to be infinite in all directions and in the numerical computations a perfectly matched absorbing layer (PML) surrounds the domain. On the boundary of the three disks we use homogeneous Dirichlet boundary conditions.

In Figure 5 we show numerically generated data recorded at the array, when the probing pulse is sent by the central array element. For comparison, we also show in Figure 5 the time traces in a homogeneous medium. Note that in the homogeneous medium (Figure 5-left) the multiple reflections that occur between the scatterers are clearly visible while in the heterogeneous medium they are lost in the multiple scattering due to the fluctuations of the background (Figure 5-center and right).

The traces for the other two probing sources look similar. The coherent interferometry images obtained for these data, using the functional equation 9, are presented in Figure 6. The domain in which we display the image is a square of size $20\lambda_0 \times 20\lambda_0$ centered on the scatterers. The optimal decoherence parameters X_d and Ω_d are chosen using the algorithm described briefly in the adaptive coherent interferometry section. As suggested by the theory, these parameters do not depend on the probing source location (when the distance to the object is not changing) and thus we use the same X_d and Ω_d for the different illuminations in the same medium. In Figure 6 we illustrate the results obtained using the left, central and right probing source. Finally, we show in Figure 7 the results given by combining the three illuminations with appropriately chosen weights.

We note that the numbers used in this example (central frequency and material properties) are relevant for non-destructive testing applications. The numerical results however are non-dimensionalized with respect to the wavelength and one can obtain a setup which is relevant for geophysics: a central frequency of 50 Hz in which

case the wavelength is 60 m and the propagation distance is of the order of 6 km.

Numerical results for coherent interferometry in randomly layered media

We present in this section imaging results obtained using the coherent interferometric functional in the case of a passive array in a randomly layered medium. Several source configurations are considered, from the simple one source case, which gives us a numerical estimation of the point spread function, to the more complex case of an extended source.

In Figure 8 we show the basic setup used in the numerical experiments in randomly layered media. The active object (source) to be imaged is embedded in a randomly fluctuating background medium with constant density and only z dependent velocity. More precisely, the variations of $c(z)$ are simulated with a random Fourier series, with mean $c_0 = 3$ km/s and a Gaussian correlation function. The correlation length is $l = 30$ m and we consider the case of strong fluctuations with strength $\sigma = 30\%$. Three realizations of the layered medium are shown in Figure 8.

The array is located near the surface, at depth $2\lambda_0$. It is composed of 41 transducers at distance $h = \lambda_0/2$ from each other. The four source configurations we consider are the following: (i) one source located at $(0, 78)$, i.e., at range $78\lambda_0$ and at zero cross-range measured with respect to the central array element, (ii) two sources located at $(0, 78)$ and $(4, 74)$ (iii) two sources located at $(0, 78)$ and $(0, 74)$, (iv) four sources located at $(0, 74)$, $(4, 74)$, $(2, 78)$ and $(-2, 78)$. All the dimensions of the problem are given in terms of the central wavelength λ_0 which is 300 m. For the extended sources we assume that all the points in the support of the source emit simultaneously at time $t = 0$ the same pulse $f(t)$ which is the time derivative of a Gaussian with central frequency $\omega_0/(2\pi) = 10$ Hz and bandwidth 6–13 Hz (measured at 6 dB).

In Figure 9 we show numerically generated time traces recorded at the array, for

one realization of the layered medium (the one shown on the left in Figure 8) and for the four source configurations considered.

The images obtained with the coherent interferometric functional are presented in Figure 10, where they are also compared with images obtained using Kirchhoff migration.

We note that the coherent interferometric images are smoother than the ones obtained with Kirchhoff migration, as the theory suggests. The parameter that controls the smoothing in the image is Ω_d (X_d is in this case the whole array aperture). Its size quantifies a trade-off between stability and resolution of the image. In the results shown in this section we use the optimal Ω_d as determined by the algorithm described in the adaptive coherent interferometry section. Assuming that Ω_d depends on the range and the random medium realization, we perform one estimation of Ω_d for the one source case and then use the same Ω_d for the other source configurations, in the same medium. In this example $\Omega_d = B/6$.

To illustrate the stability of the coherent interferometry we show in Figure 11 imaging results obtained for three different realizations of the randomly layered medium and for the configuration with four sources. In practice the decoherence frequency Ω_d is not very sensitive on the particular realization of the random medium considered. In all the examples shown in Figure 11 $\Omega_d \approx B/6$ with a variance of 5%. The obtained image does not change significantly for small variations of Ω_d . It does change, however, for larger variations of Ω_d as for $\Omega_d = B$ one obtains the Kirchhoff migration results and for Ω_d very small one would obtain an overly smoothed image.

Let us first note that the random shift in range is as predicted by the well known O'Doherty-Anstey theory (O'Doherty and Anstey, 1971). This shift seems to be constant along the array elements in these experiments as the array aperture is small compared to the range. Note also that different shifts are observed for different realizations of the layered medium. The trade-off between stability and resolution is clearly seen in Figure 11. The images obtained using coherent interferometry are

consistently good and the four sources are reconstructed with the same quality in resolution for all the realizations of the random medium. However, for Kirchhoff migration the reconstruction depends on the realization of the layered medium. A good and tight image is obtained, for example, for the second realization of the random medium (right image, first row) as opposed to the other two where the sources in the back are poorly reconstructed.

ADAPTIVE COHERENT INTERFEROMETRY

The coherent interferometric functional equation 9 depends in an essential way on the choice of the smoothing or coherence parameters X_d and Ω_d . We see this clearly in the numerical simulations shown in Figure 12 for the isotropic random medium, and Figure 10 and 11 for randomly layered media. This is particularly clear in Figure 12 where we see the way the choice of X_d and Ω_d quantifies the trade-off between statistical stability and blurring. When there is no smoothing, as in Kirchhoff migration on the top in Figure 12, the images depend on the realization of the random medium (top left and right in Figure 12). No smoothing means that $\Omega_d = B$, the full bandwidth, and $X_d = a$, the full array, in equation 9. This makes the coherent interferometric functional equation 9 simply the square of the Kirchhoff migration functional equation 5. When there is too much smoothing, that is, X_d and Ω_d are too small, then there is too much blurring as on the bottom in Figure 12. Note, however, the statistical stability of the blurred image in this case, for there is little difference between the blurred images for the two realizations (bottom left and right in Figure 12). When the smoothing or decoherence parameters X_d and Ω_d are chosen optimally then we get statistically stable images that are blurred minimally, as shown in the central panel of Figure 12.

How do we select the smoothing or decoherence parameters X_d and Ω_d so as to get the optimal trade-off between statistical stability and blurring? There are many ways

to do this, and we experimented with several possibilities. We have found that (a) the selection of X_d and Ω_d should be done based on the image as it is being formed, and (b) a feature preserving norm should be used, such as the bounded variation or the entropy. In our work we use the bounded variation (BV) norm of the image function (Giusti, 1984)

$$\|\mathcal{I}^{\text{CINT}}(\cdot, X_d, \Omega_d)\|_{BV} = \int_{\mathcal{D}} |\nabla \mathcal{I}^{\text{CINT}}(\mathbf{y}^s, X_d, \Omega_d)| d\mathbf{y}^s + \int \mathcal{D} |\mathcal{I}^{\text{CINT}}(\mathbf{y}^s, X_d, \Omega_d)| d\mathbf{y}^s \quad (13)$$

where the integration is done over a suitable region \mathcal{D} around the object to be imaged and where $\mathcal{I}^{\text{CINT}}$ is normalized by its maximal value in \mathcal{D} . In practice, region \mathcal{D} is a few wavelengths in diameter (20λ in the examples considered in this paper). The smoothing parameters are chosen iteratively to minimize this norm. In this way large scale features of the image are preserved, and the BV norm is essential for this, while the noise is smoothed out. This is a new way to use the bounded variation norm in imaging, or more accurately in image formation. It is very commonly used in image deblurring, which is something that can be done here too (Borcea et al., 2005a) once a stable-but-blurred image is formed, as in Figure 12 at center. But the use of the bounded variation norm to smooth Kirchhoff migration with coherent interferometry, as in equations 9, 13, is new and seems to be quite effective.

To solve the minimization one can use a code such as steepest descent. In the results presented in this paper, however, we used the NOMADm software package (Audet and Dennis, 2003; Abramson, 2002) for constrained, nonlinear, mixed variable problems, that uses a mesh-adaptive direct search method. In practice, because the BV norm may possess local minima, we first do some coarse grid search to find out from where to start the minimization algorithm.

We note that in the case of isotropic clutter the resolution of the coherent interferometry depends on X_d and not on the actual array size. We have shown in (Borcea et al., 2005b) that the sum $\bar{\mathbf{x}}_r^\perp \in \mathcal{A}$ has an influence only on the stability of the image and not on its resolution. Moreover, what appears to be more important for the sta-

bility is the averaging over frequency provided by the integral $|\bar{\omega} - \omega_0| \in B$. We may conclude, therefore, that the size of the array is not so important when imaging in isotropic clutter. In the layered case, however, X_d is infinite so the array size becomes important.

CONCLUSIONS

We have shown that the coherent interferometric functional, along with an optimal selection of the smoothing parameters X_d and Ω_d that minimize the bounded variation norm of the interferometric image, gives very good results in cluttered environments. At the same time, the optimal smoothing parameters characterize the resolution of the image obtained in a direct and simple manner. The range resolution is proportional to c_o/Ω_d and the cross-range resolution is proportional to $c_oL/(BX_d)$. This is to be contrasted with the resolution in Kirchhoff migration in a homogeneous medium where we have range and cross-range resolutions proportional to c_o/B and $c_oL/(Ba)$, respectively. Since in cluttered media the decoherence frequency Ω_d and the decoherence distance X_d are usually much smaller than the bandwidth B and the array size a , respectively, we see clearly the loss of resolution due to the clutter. Moreover, it is with the image formation process itself, when using coherent interferometry, that we get the best estimates for these two parameters that characterize so well the effect of the clutter on the image.

ACKNOWLEDGMENT

The work of L. Borcea was partially supported by the Office of Naval Research, under grant N00014-02-1-0088 and by the National Science Foundation, grants DMS-0305056, DMS-0354658. The work of G. Papanicolaou was supported by grants ONR N00014-02-1-0088 and 02-SC-ARO-1067-MOD 1. The work of C. Tsogka was partially

supported by the Office of Naval Research, under grant N00014-02-1-0088 and by 02-SC-ARO-1067-MOD 1.

REFERENCES

- Abramson, M., 2002, Pattern search algorithms for mixed variable general constrained optimization problems: PhD thesis, Rice University. Software available at: <http://en.afit.edu/ENC/Faculty/MAbramson/abramson.html>.
- Audet, C. and J. Dennis, 2000, Revised November 2003, A pattern search filter method for nonlinear programming without derivatives: Technical report, Rice University, <http://www.caam.rice.edu>.
- Baggeroer, A., W. Kuperman, and P. Mikhalevsky, 1993, An overview of matched field methods in ocean acoustics: *IEEE Journal of Ocean Engineering*, **18**, 401–424.
- Bal, G., G. Papanicolaou, and L. Ryzhik, 2002, Self-averaging in time reversal for the parabolic wave equation: *Stochastics and Dynamics*, **2**, 507–531.
- Bal, G. and L. Ryzhik, 2003, Time reversal and refocusing in random media: *SIAM Journal on Applied Mathematics*, **63**, 1475–1498.
- Bécache, E., P. Joly, and C. Tsogka, 2000, An analysis of new mixed finite elements for the approximation of wave propagation problems: *SIAM Journal on Numerical Analysis*, **37**, 1053–1084.
- Beylkin, G., 1985, Imaging of discontinuities in the inverse scattering problem by inversion of a causal generalized Radon transform: *J. Math. Phys.*, **26**, 99–108.
- Beylkin, G. and R. Burridge, 1990, Linearized inverse scattering problems in acoustics and elasticity: *Wave Motion*, **12**, 15–52.
- Bleistein, N., J. Cohen, and J. S. Jr., 2001, *Mathematics of multidimensional seismic imaging, migration, and inversion*: Springer, New York.

- Blomgren, P., G. Papanicolaou, and H. Zhao, 2002, Super-resolution in time-reversal acoustics: *Journal of the Acoustical Society of America*, **111**, 238–248.
- Borcea, L., G. Papanicolaou, and C. Tsogka, 2003, Theory and applications of time reversal and interferometric imaging: *Inverse Problems*, **19**, S134–164.
- 2005a, Adaptive coherent interferometry in clutter: *Inverse Problems*, submitted.
- 2005b, Interferometric array imaging in clutter: *Inverse Problems*, **21**, 1419–1460.
- Borcea, L., G. Papanicolaou, C. Tsogka, and J. Berryman, 2002a, Imaging and time reversal in random media: *Inverse Problems*, **18**, 1247–1279.
- 2002b, Statistically stable ultrasonic imaging in random media: *Journal of the Acoustical Society of America*, **112**, 1509–1522.
- Bucker, H. P., 1976, Use of calculated sound field and matched-field detection to locate sound sources in shallow water: *Journal of the Acoustical Society of America*, **59**, 368–373.
- Carazzone, J. and W. Symes, 1991, Velocity inversion by differential semblance optimization: *Geophysics*, **56**, 654–663.
- Chan, T. K., Y. Kuga, and A. Ishimaru, 1999, Experimental studies on circular sar imaging in clutter using angular correlation function technique: *IEEE Transactions in Geoscience and Remote Sensing*, **37**, 2192–2197.
- Claerbout, J., 1968, Synthesis of a layered medium from its acoustic transmission response: *Geophysics*, **33**, 264–269.
- 1985, *Fundamentals of geophysical data processing : with applications to petroleum prospecting*: CA : Blackwell Scientific Publications, Palo Alto.
- Claerbout, J. and S. Doherty, 1972, Downward continuation of moveout-corrected seismograms: *Geophysics*, **37**, 741–768.

- Clouet, J. F. and J. Fouque, 1997, A time reversal method for an acoustical pulse propagating in randomly layered media: *Wave Motion*, **25**, 361–368.
- Cole, S., 1995, Passive seismic and drill-bit experiments using 2-d arrays: PhD thesis, Stanford University.
- Derode, A., P. Roux, and M. Fink, 1995, Robust acoustic time reversal with high-order multiple scattering: *Physical Review Letters*, **75**, 4206–4209.
- Fink, M., 1993, Time reversal mirrors: *Journal of Physics D*, **26**, 1330–1350.
- 1997, Time reversed acoustics: *Physics Today*, **50**, 34–40.
- Fink, M., D. Cassereau, A. Derode, C. Prada, P. Roux, and M. Tanter, 2000, Time-reversed acoustics: *Reports on Progress in Physics*, **63**, 1933–1994.
- Fouque, J. P., S. Garnier, A. Nachbin, and K. Solna, 2005, Time reversal refocusing for a point source in randomly layered media: *Wave Motion*, **42**, 191–288.
- Fouque, J. P. and K. Solna, 2003, Time reversal aperture enhancement: *SIAM Multiscale Modeling and Simulation*, **1**, 239–259.
- Giusti, E., 1984, *Minimal Surfaces and Functions of Bounded Variation*: Birkhäuser.
- Gockenbach, M., 1994, An abstract analysis of differential semblance optimization: PhD thesis, Rice University.
- Krolik, J., 1992, Matched field minimum-variance beamforming in random ocean channel: *Journal of the Acoustical Society of America*, **92**, 1408–1419.
- Kroode, A. T., D. Smit, and A. Verdel, 1998, A microlocal analysis of migration: *Wave Motion*, **28**, 149–172.
- Lobkis, O. and R. Weaver, 2001, On the emergence of the Green’s function in the correlations of a diffuse field: *Journal of the Acoustical Society of America*, **110**, 3011–3017.

- Nolan, C. and W. Symes, 1997, Global solution of a linearized inverse problem for the wave equation: *Communications in Partial Differential Equations*, **22**, 919–952.
- O’Doherty, R. and N. Anstey, 1971, Reflections on amplitudes: *Geophysical Prospecting*, **19**, 430–458.
- Papanicolaou, G., L. Ryzhik, and K. Solna, 2004, Statistical stability in time reversal: *SIAM Journal on Applied Mathematics*, **64**, 1133–1155.
- Priestley, M. B., 1981, *Spectral analysis and time series*: Academic Press.
- Rickett, J. and J. Claerbout, 1999, Acoustic daylight imaging via spectral factorization: *Helioseismology and reservoir monitoring: The leading edge*, **18**, 957–960.
- Schultz, P. and J. Claerbout, 1978, Velocity estimation and downward-continuation by wavefront synthesis: *Geophysics*, **43**, 691–714.
- Schuster, G. T., J. Yu, J. Sheng, and J. Rickett, 2004, Interferometric/daylight seismic imaging: *Geophysics Journal International*, **157**, 838–852.
- Sheng, J. and G. T. Schuster, 2003, Finite-frequency resolution limits of wave path traveltimes tomography for smoothly varying velocity models: *Geophysics Journal International*, **152**, 669–676.
- Snieder, R., 2004, Extracting the Green’s function from the correlation of coda waves: A derivation based on stationary phase: *Physical Review E*, **69**, 46610–46618.
- Solna, K., 2002, Focusing of time-reversed reflections: *Waves Random Media*, **12**, 365–385.
- Song, H., W. Kuperman, and W. Hodgkiss, 1999, Iterative time reversal in the ocean: *Journal of the Acoustical Society of America*, **105**, 3176–3184.
- Stolk, C. and M. deHoop, 2002, Microlocal analysis of seismic inverse scattering in anisotropic elastic media: *Communications in Pure and Applied Mathematics*, **55**, 261–301.

- Stolk, C. and W. Symes, 2003, Smooth objective functionals for seismic velocity inversion: *Inverse Problems*, **19**, 73–89.
- Symes, W., 1991, Layered velocity inversion: a model problem from reflection seismology: *SIAM Journal on Mathematical Analysis*, **22**, 680–716.
- 1993, A differential semblance criterion for inversion of multioffset seismic reflection data: *Journal of Geophysical Research*, **88**, 2061–2074.
- Uscinski, B. J., 1985, Analytical solution of the fourth-moment equation and interpretation as a set of phase screens: *Journal of the Optical Society of America*, **2**, 2077–2091.

FIGURES

Figure 1. Schematic for passive (left) and active array imaging(right)

Figure 2. Acoustic velocity profile measured in a well log.

Figure 3. An illustration, from ultrasonic non-destructive testing, of an isotropic cluttered medium. The speed of the waves in the clutter varies randomly about the constant value of 3 km/s. The vertical and horizontal axes are range and cross-range in units of carrier wavelength λ_o .

Figure 4. The computational setup. The dimensions of the problem are given in terms of the central wavelength λ_o . The array elements are indicated by the tiny boxes at the top.

Figure 5. Time traces recorded on the array in a homogeneous background (left) and in random background medium with standard deviation $\sigma = 3\%$ and correlation function equation 11 (middle) and equation 12 (right). The horizontal axis is array transducer location scaled by λ_o and the vertical is time scaled by the pulse-width.

Figure 6. Coherent interferometric images for the three probing sources left, central and right (from top to bottom) in a random medium with the Gaussian correlation function (left column) and the multiscale correlation function (right column). The vertical and horizontal axes are range and cross-range in units of carrier wavelength λ_o . The true support of the scatterers is indicated by black dots.

Figure 7. Coherent interferometric images with optimal weighting of the illuminations. Left: medium with Gaussian correlation function and right: medium with the multiscale correlation function. The vertical and horizontal axes are range and

cross-range in units of carrier wavelength λ_o . The true support of the scatterers is indicated by black dots.

Figure 8. The setup for the numerical simulations in a randomly layered medium. We show on the left the extended source configuration, composed of four point sources located at $(0, 74)$, $(4, 74)$, $(2, 78)$, $(-2, 78)$. The length units are in terms of the carrier wavelength λ_o and the distance d is 4. The array is composed of 41 transducers at a distance $h = \lambda_o/2$ apart, with the central transducer located at point $(0, 2)$. The two other figures (middle and right) correspond to two other realizations of the layered medium.

Figure 9. Traces recorded across the array from left to right: for a single source, two sources one behind the other, two sources located at $(0, 78)$ and $(4, 74)$ and four sources. The ordinate in the pictures is time scaled by the pulse-width and the abscissa is the array element position in λ_o .

Figure 10. Images obtained using Kirchhoff migration on the top row and CINT on the bottom one. From left to right: single source, two sources one behind the other, two sources located at $(0, 78)$ and $(4, 74)$ and four sources. The vertical and horizontal axes are range and cross-range in units of carrier wavelength λ_o . The true support of the sources is indicated by green dots.

Figure 11. Migration images of four sources for three realizations of the random medium. Top: Kirchhoff migration. Bottom: Coherent Interferometry. The vertical and horizontal axes are range and cross-range in units of carrier wavelength λ_o . The true support of the sources is indicated by green dots.

Figure 12. Coherent Interferometry images in isotropic random media with $s = 3\%$

and Gaussian correlation function equation 11. Two different realizations are shown in the left and right columns, with Kirchhoff migration on the top, coherent interferometry with optimal selection of X_d and Ω_d in the middle, and sub-optimal selection that smooths too much on the bottom. The vertical and horizontal axes are range and cross-range in units of carrier wavelength λ_o . The true support of the scatterers is indicated by black dots.

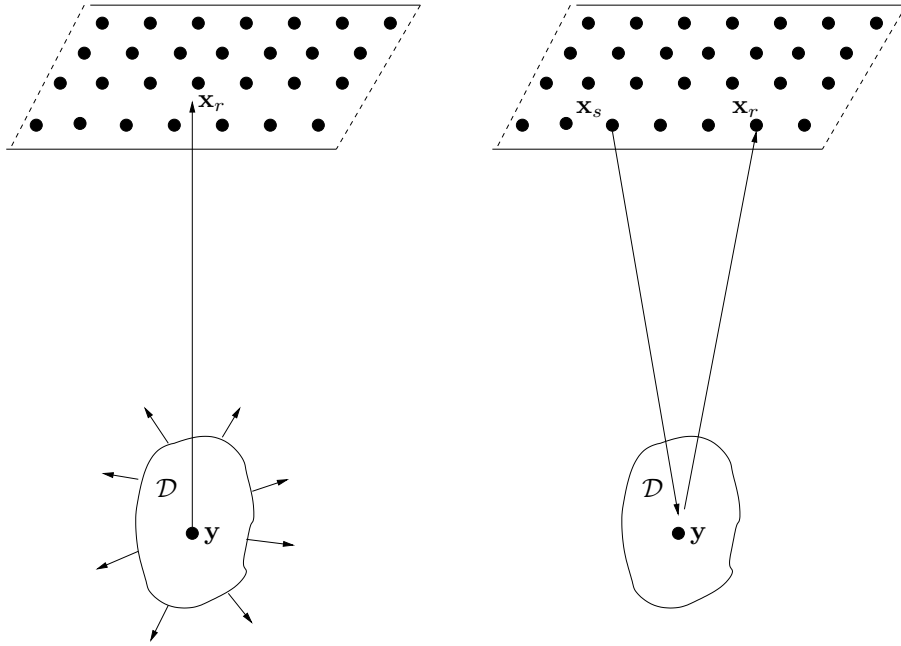


Figure 1. Schematic for passive (left) and active array imaging(right)

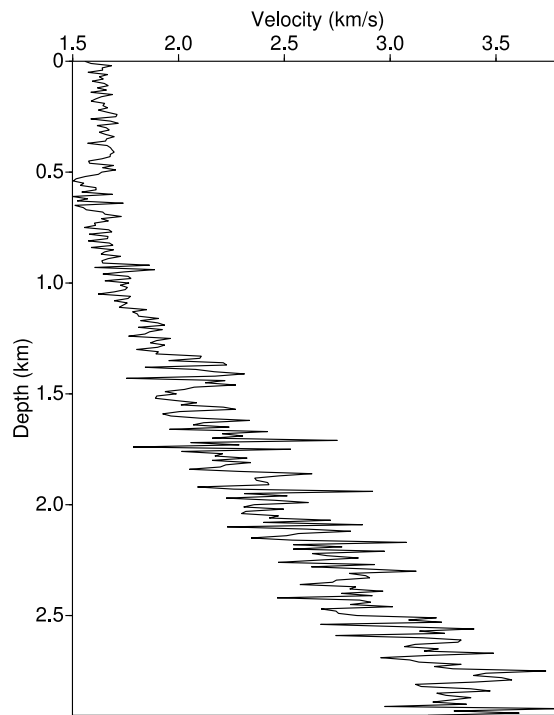


Figure 2. Acoustic velocity profile measured in a well log.

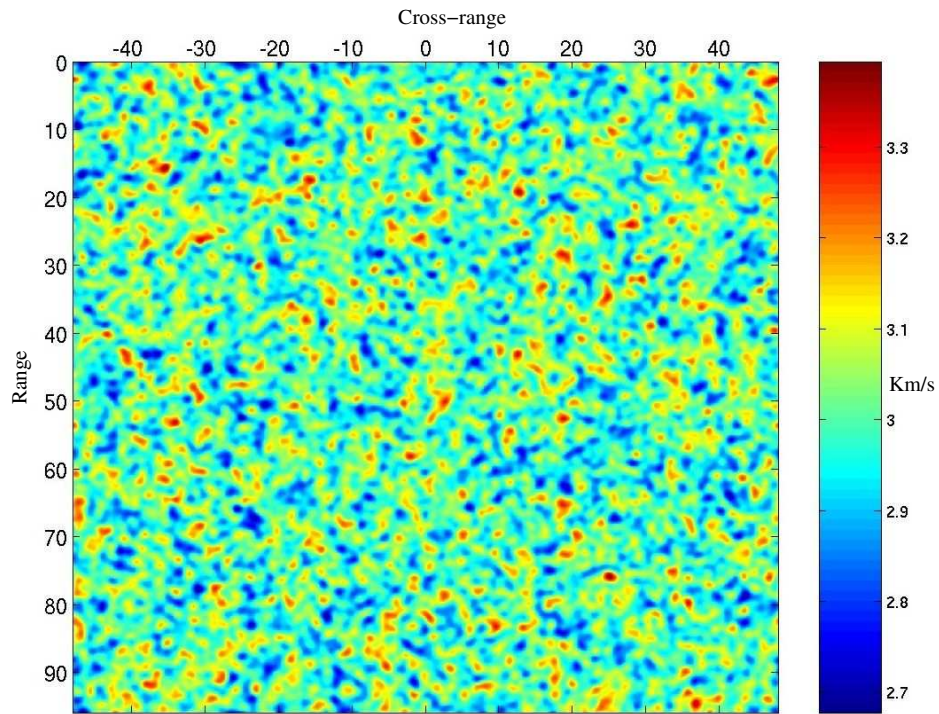


Figure 3. An illustration, from ultrasonic non-destructive testing, of an isotropic cluttered medium. The speed of the waves in the clutter varies randomly about the constant value of 3 km/s. The vertical and horizontal axes are range and cross-range in units of carrier wavelength λ_o .

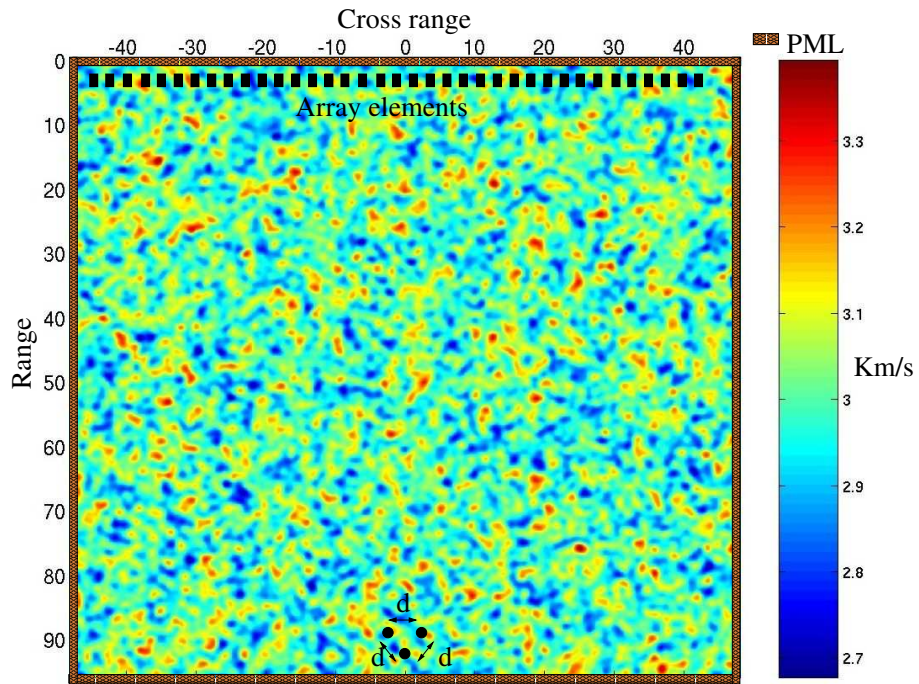


Figure 4. The computational setup. The dimensions of the problem are given in terms of the central wavelength λ_0 . The array elements are indicated by the tiny boxes at the top.

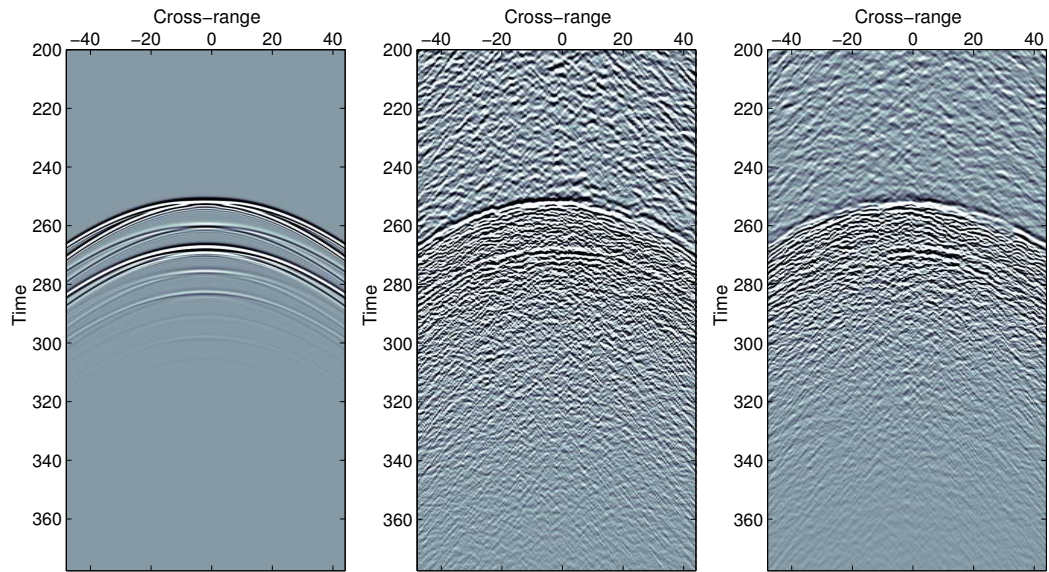


Figure 5. Time traces recorded on the array in a homogeneous background (left) and in random background medium with standard deviation $\sigma = 3\%$ and correlation function equation 11 (middle) and equation 12 (right). The horizontal axis is array transducer location scaled by λ_0 and the vertical is time scaled by the pulse-width.

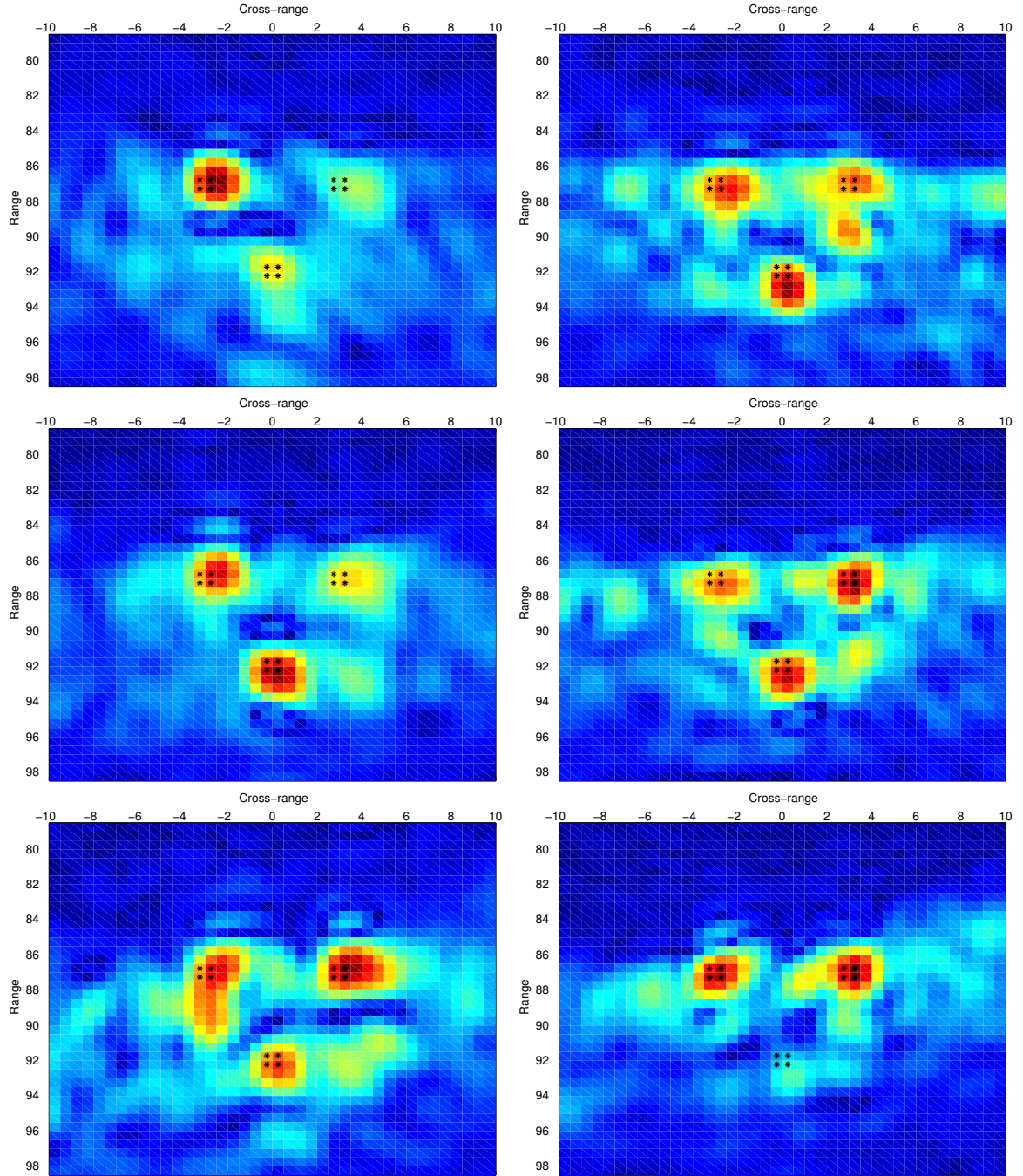


Figure 6. Coherent interferometric images for the three probing sources left, central and right (from top to bottom) in a random medium with the Gaussian correlation function (left column) and the multiscale correlation function (right column). The vertical and horizontal axes are range and cross-range in units of carrier wavelength λ_o . The true support of the scatterers is indicated by black dots.

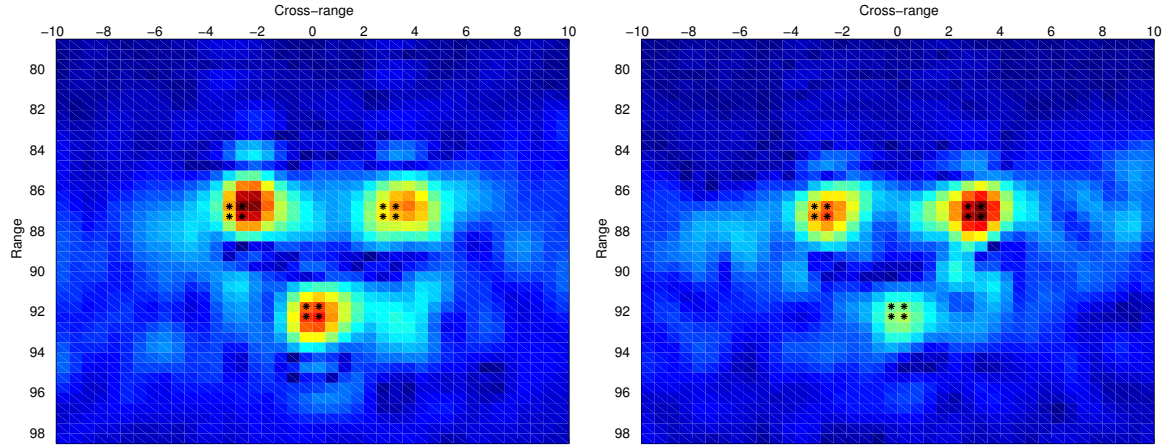


Figure 7. Coherent interferometric images with optimal weighing of the illuminations. Left: medium with Gaussian correlation function and right: medium with the multiscale correlation function. The vertical and horizontal axes are range and cross-range in units of carrier wavelength λ_o . The true support of the scatterers is indicated by black dots.

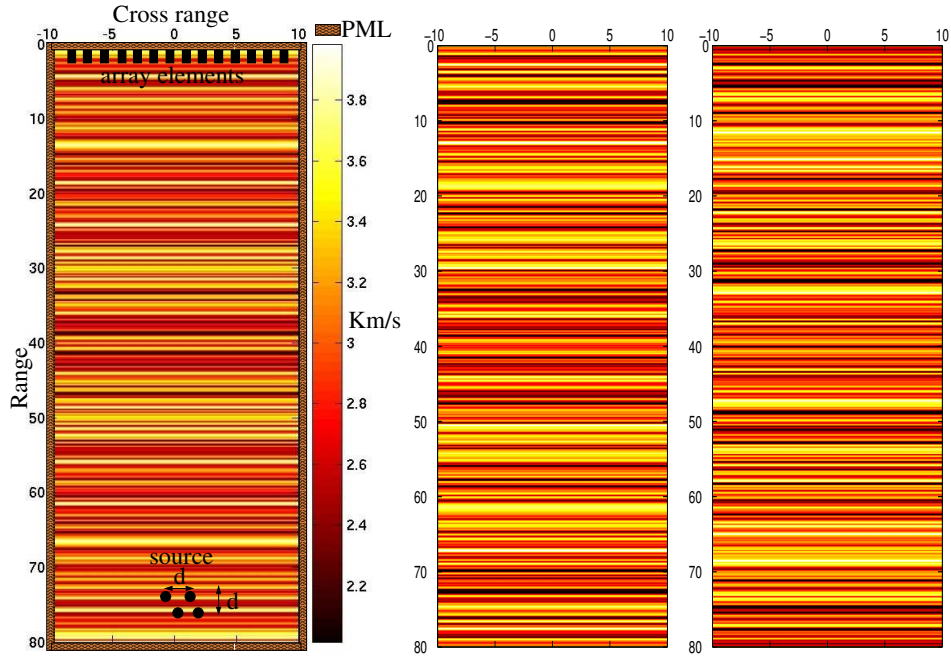


Figure 8. The setup for the numerical simulations in a randomly layered medium. We show on the left the extended source configuration, composed of four point sources located at $(0, 74)$, $(4, 74)$, $(2, 78)$, $(-2, 78)$. The length units are in terms of the carrier wavelength λ_0 and the distance d is 4. The array is composed of 41 transducers at a distance $h = \lambda_0/2$ apart, with the central transducer located at point $(0, 2)$. The two other figures (middle and right) correspond to two other realizations of the layered medium.

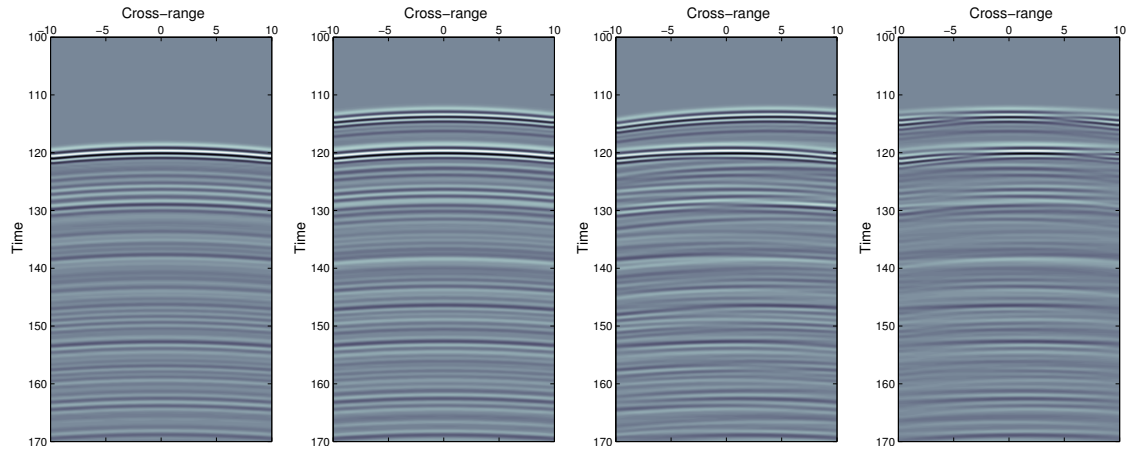


Figure 9. Traces recorded across the array from left to right: for a single source, two sources one behind the other, two sources located at $(0, 78)$ and $(4, 74)$ and four sources. The ordinate in the pictures is time scaled by the pulse-width and the abscissa is the array element position in λ_0 .

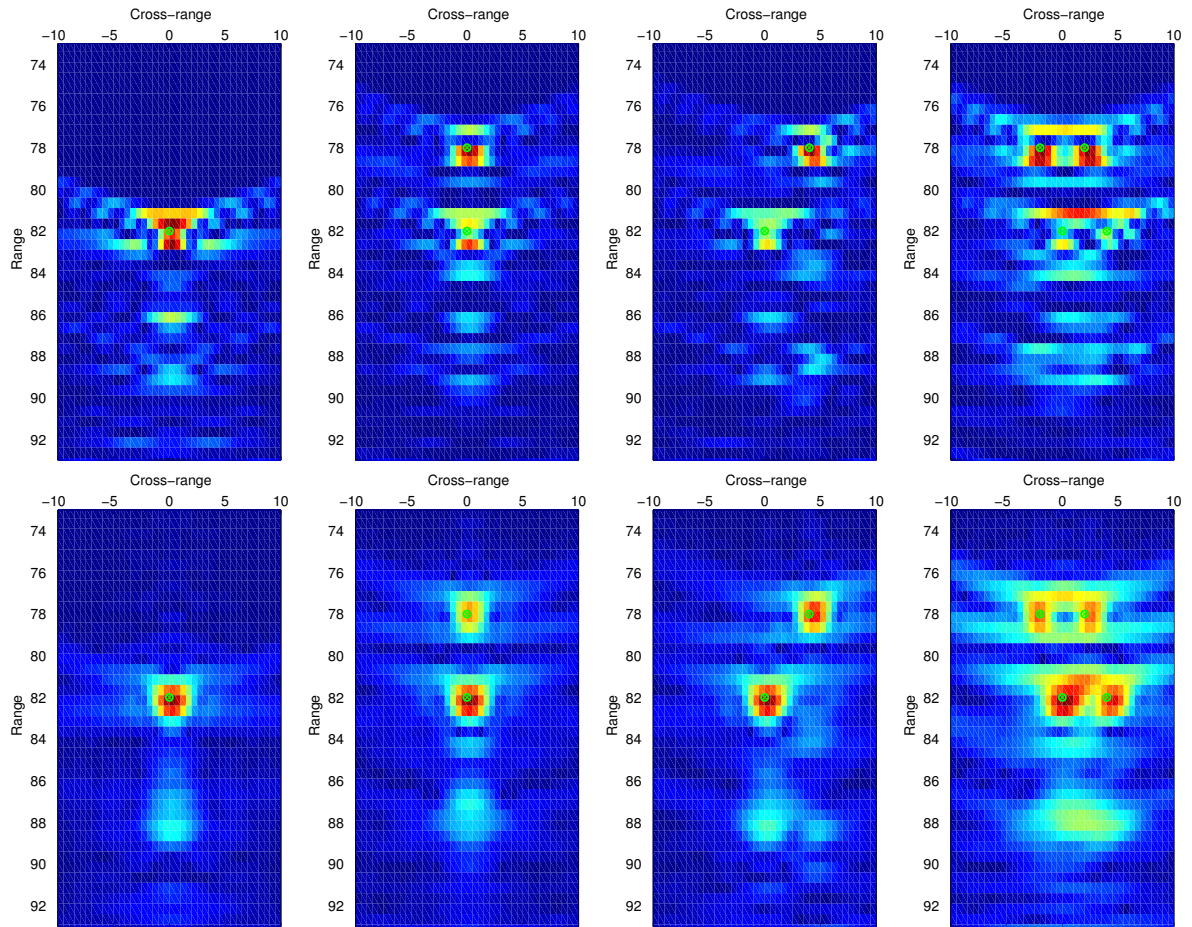


Figure 10. Images obtained using Kirchhoff migration on the top row and CINT on the bottom one. From left to right: single source, two sources one behind the other, two sources located at $(0, 78)$ and $(4, 74)$ and four sources. The vertical and horizontal axes are range and cross-range in units of carrier wavelength λ_o . The true support of the sources is indicated by green dots.

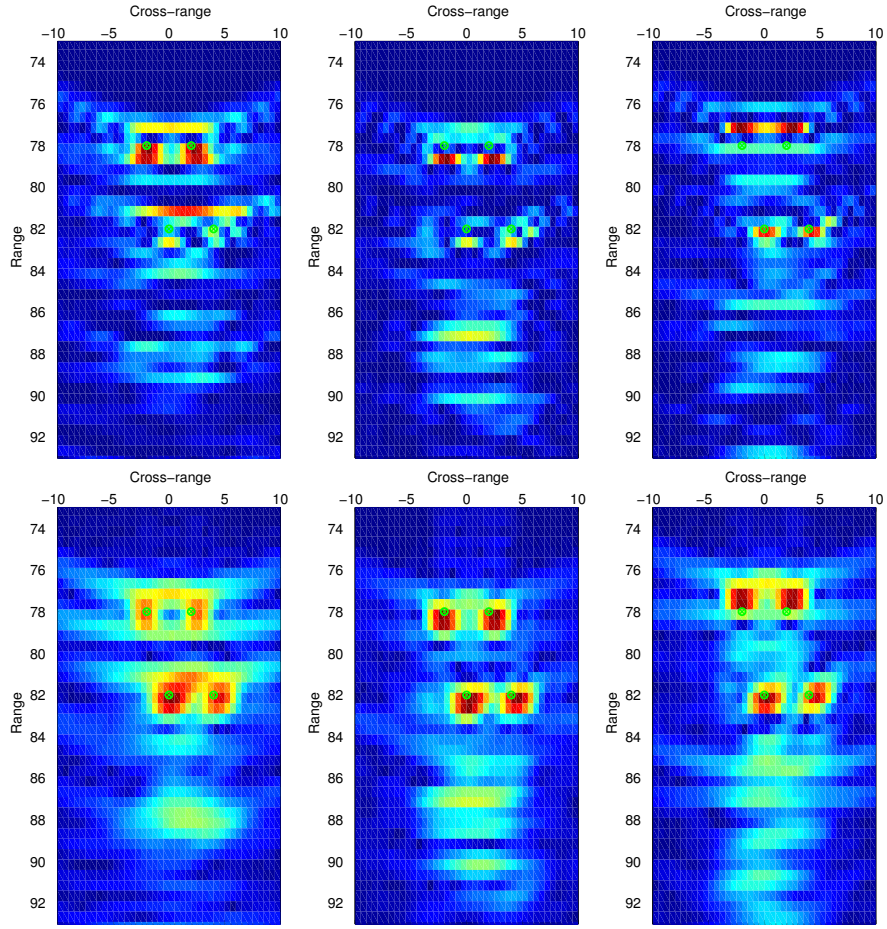


Figure 11. Migration images of four sources for three realizations of the random medium. Top: Kirchhoff migration. Bottom: Coherent Interferometry. The vertical and horizontal axes are range and cross-range in units of carrier wavelength λ_o . The true support of the sources is indicated by green dots.

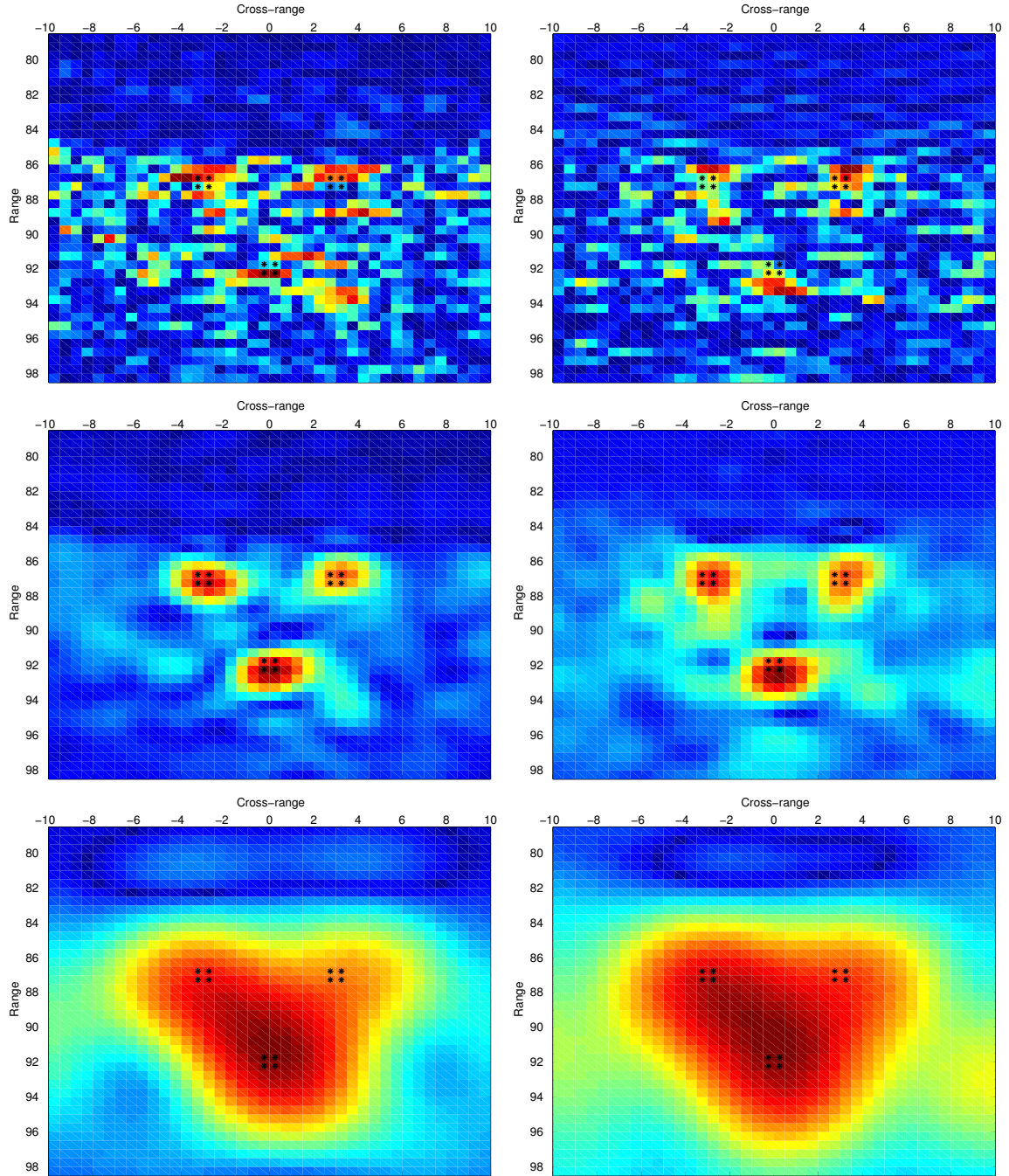


Figure 12. Coherent Interferometry images in isotropic random media with $s = 3\%$ and Gaussian correlation function equation 11. Two different realizations are shown in the left and right columns, with Kirchhoff migration on the top, coherent interferometry with optimal selection of X_d and Ω_d in the middle, and sub-optimal selection that smooths too much on the bottom. The vertical and horizontal axes are range and cross-range in units of carrier wavelength λ_o . The true support of the scatterers is indicated by black dots.